Atmospheric Environment 319 (2024) 120292

Contents lists available at ScienceDirect

Atmospheric Environment

journal homepage: www.elsevier.com/locate/atmosenv

A seven-year-based characterization of aerosol light scattering properties at a rural central European site

Lenka Suchánková [a,b,c,*], Saliou Mbengue [b], Naděžda Zíková [c], Adéla Holubová Šmejkalová [d], Roman Prokeš [a,b], Ivan Holoubek [a,b], Vladimír Ždímal [c]

[a] RECETOX, Faculty of Science, Masaryk University, Brno, 611 37, Czech Republic
[b] Global Change Research Institute of the Czech Academy of Sciences, Brno, 603 00, Czech Republic
[c] Institute of Chemical Process Fundamentals of the Czech Academy of Sciences, Prague, 165 02, Czech Republic
[d] Czech Hydrometeorological Institute, Na Šabatce 2050/17, Praha 4-Komořany, 143 06, Czech Republic

HIGHLIGHTS

- 7-year-based measurement of σ_{sp} and σ_{bsp} and climate-relevant variables (*SAE, b, g*) were analyzed at a rural background.
- Decreasing σ_{sp} σ_{bsp} and *SAE* suggests a shift to larger particles with a higher backscatter fraction.
- Variability of aerosol light scattering properties were investigated during different fog events and cloudiness categories.

GRAPHICAL ABSTRACT

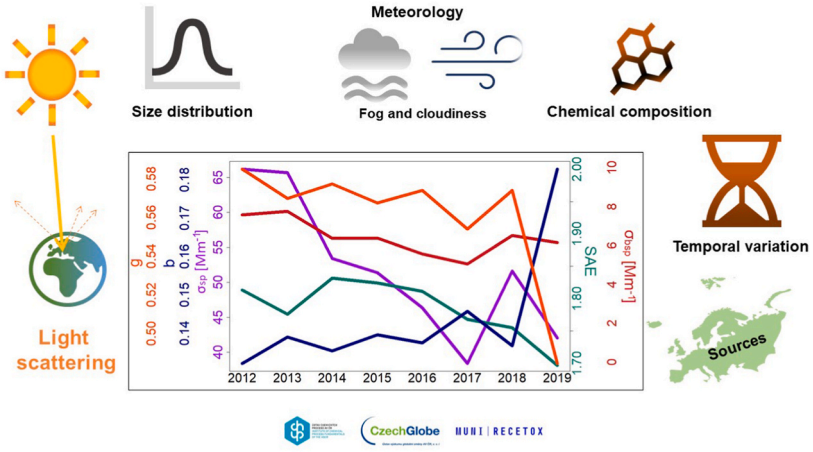

ARTICLE INFO

Keywords:
Aerosol optical properties
Scattering coefficient
Nephelometer
Long-term temporal variations

ABSTRACT

Our study investigates the temporal variability of aerosol light scattering properties measured at three wavelengths (total scattering coefficient, backscattering coefficient, Ångström scattering exponent, hemispheric backscattering ratio and asymmetry parameter) at the rural background site of the National Atmospheric Observatory Košetice over a period of over seven years (2012–2019). The influence of fog and cloudiness on aerosol light scattering properties (ASP), together with their comparison to particle number size distribution was also investigated. The overall medians of total scattering (σ_{sp}) and backscattering coefficient (σ_{bsp}), hemispheric backscattering ratio (*b*) and asymmetry parameter (*g*) measured at 550 nm and Ångström scattering exponent (*SAE_450/700*) were 35.20 Mm^{-1}, 5.07 Mm^{-1}, 0.14 and 0.57 and 1.82, respectively. σ_{sp} and *g* decreased by 2.05 Mm^{-1}/year, and 0.009/year, respectively, whereas *b* increased by 0.004/year. The selected aerosol properties were strongly correlated with particle number, mass, area and volume concentrations in the 200–800 nm mode.

* Corresponding author. RECETOX, Faculty of Science, Masaryk University, Brno, 611 37, Czech Republic.
E-mail address: suchankova.l@czechglobe.cz (L. Suchánková).

https://doi.org/10.1016/j.atmosenv.2023.120292
Received 11 July 2023; Received in revised form 7 December 2023; Accepted 10 December 2023
Available online 15 December 2023

A decrease in *SAE*_450/700 implies a shift towards larger particle sizes, and evolutions in *b* and *g* suggest a higher backscattering portion to total scattering. The highest σ_{sp} and σ_{bsp} levels were observed in the cold seasons together with higher concentrations of air pollutants (carbonaceous aerosol, SO_2 and NO_x). This could be explained by enhanced emissions from human activities such as domestic heating combined with the higher stability of the atmosphere (poor atmospheric dispersion). In the summer, decreases in particle size and higher rates of backscatter fraction were attributed to secondary organic aerosol (SOA) formation. The accumulation mode showed the strongest aerosol scattering potential, with *SAE*_450/700 values < 2. Aerosol light scattering was significantly higher during overcast and foggy days compared to fine, cloudy, partly cloudy and no-fog days, possibly due to the particle hygroscopic growth under high relative humidity (shift of particle size towards larger sizes), which in turn can lead to a lower aerosol backscattering fraction. Source identification linked the changes in ASP to the synoptic situation over Europe rather than to specific sources of pollution.

1. Introduction

Atmospheric aerosols significantly influence the Earth's radiative forcing (Bäumer et al., 2008; Koschmieder, 1924). They directly impact the Earth's climate system by the scattering or absorption of incoming solar and outgoing infrared radiation, and indirectly by modifying cloud properties and their lifespan (Boucher, 2015; Charlson et al., 1992; Hansen et al., 1997; IPCC, 2021; Luoma et al., 2019; Ramanathan et al., 2001). The direct aerosol radiative forcing effect consists of both warming and cooling effects (IPCC, 2021; Pandolfi et al., 2018; Seinfeld and Pandis, 2006). Black carbon particles, as the second most significant agents in terms of warming and climate-radiative forcing after carbon dioxide, absorb radiation (Bond et al., 2013). However, the dominant cooling effect originates from the scattering of radiation by specific atmospheric aerosols by reducing the amount of solar radiation attaining the Earth's surface (IPCC, 2021). This cooling effect counterbalances the greenhouse effect and modifies the Earth's radiative forcing (Pandolfi et al., 2018). The reduction of emissions of anthropogenic aerosol particles has led to a decrease in the cooling effect of aerosols in the atmosphere (Quaas et al., 2022). Despite this, aerosol radiative forcing remains a major source of uncertainty in estimating climate change due to the high spatial and temporal variations of chemical and physical properties, shorter lifetime in comparison to greenhouse gases, and variety of aerosol sources (Boucher, 2015; Lee et al., 2016; Luoma et al., 2019).

The reasons behind the large uncertainty in the modeling of aerosol radiative forcing are not yet fully understood. To address this knowledge gap, several international monitoring programs have been established to harmonize measurements of aerosol optical properties (AOP), such as light scattering and absorption, across various infrastructures around the world (Pandolfi et al., 2018). Long-term observations of aerosol light scattering properties (ASP) in different environments are essential for better understanding aerosol behavior and evaluating their local, regional, and global impacts on climate change (Delene and Ogren, 2002; Sheridan et al., 2001).

Although various studies on the aerosol scattering properties (Laj et al., 2020; Luoma et al., 2019; Pandolfi et al., 2018; Rama Gopal et al., 2014; Schmeisser et al., 2018; Van Dingenen et al., 2004) as well as studies on broader range or aerosol properties including scattering (Andrews et al., 2011; Collaud Coen et al., 2020; Donateo et al., 2020) have been published in recent years, there is a scarcity of long-term series measured at rural background sites.

Therefore, the aim of this study is to describe the light scattering properties of aerosols at the National Atmospheric Observatory Košetice (NAOK), a rural background station in Central Europe, based on seven years of measurements. In this work, detailed annual, seasonal, monthly, and diurnal patterns of ASP are characterized with respect to other aerosol properties, air pollutants, meteorological conditions, and the origin of potential sources. This study will contribute to strengthening of our knowledge of the optical properties and emission sources of light scattering aerosol particles at European rural background sites.

2. Materials and methods

2.1. Experimental site

The NAOK (49°34′24″ N, 15°4′49″ E, 534 m a.s.l.), classified as a rural background site, is located in the central Czech Republic (Fig. 1) in the Bohemian-Moravian Highlands. It is influenced by aerosols from both regional origins and long-range transport associated with continental and marine air masses (Dvorská et al., 2015; Mbengue et al., 2018, 2021; Ramonet et al., 2020; Schwarz et al., 2016; Shahpoury et al., 2015; Vodička et al., 2015; Zíková and Ždímal, 2013). The surrounding landscape consists mainly of agricultural fields with partial forest cover, located approx. 60 km SE of the capital city of Prague. Found nearby are the villages of Košetice (3 km SE, population of 721 citizens; CSO, 2022) and Kramolín (1.2 km SW, population of 125 citizens; CSO, 2022). A major Czech highway D1 (part of E50/E65) is approx. 7 km NE (with around 36,000 cars per day; RSD, 2020), and the closest main road is 1 km E (approx. 1300 cars per day; RSD, 2020). A manufacturer of sawn timber and wood-based board materials, one of the main polluters in the region with formaldehyde as the main emission could be found 7.5 km west of the site (Holubová Šmejkalová et al., 2021; Mbengue et al., 2021).

NAOK has been involved in several monitoring projects and programs such as the Aerosol, Clouds and Trace Gases Research Infrastructure Network (ACTRIS ERIC) and its Czech counterpart ACTRIS-CZ, the Integrated Carbon Observation System (ICOS ERIC), the large research infrastructure CzeCOS, the European Monitoring and Evaluation Programme (EMEP), the Global Mercury Observation System (GMOS), the Global Atmosphere Watch (GAW), the Czech Air Quality Information System Database (ISKO), Aeronet, and others (Mbengue et al., 2021).

2.2. Measurement of extensive scattering properties

Measurements of ASP have been widely conducted using nephelometers, which use a non-destructive method to measure directly in the in the atmosphere two extensive properties of aerosol light scattering: total scattering coefficient σ_{sp} and hemispheric backscattering coefficient σ_{bsp} (Pandolfi et al., 2018; Rajesh and Ramachandran, 2020). σ_{sp} quantifies total scattered radiation by particle at all angles, while σ_{bsp} quantifies the amount of scattered light into the hemisphere of space at 90°–180° to the original direction of radiative flux (Anderson et al., 1999).

The measurement data in this study were continuously collected from August 16, 2012, to December 31, 2019. σ_{sp} and σ_{bsp} were measured at three wavelengths (450, 550 and 700 nm) using the Integrating Nephelometer TSI 3563 (TSI Incorporated, USA) (Anderson and Ogren, 1998). Sampling was carried out at 5-min intervals from August 2012 to February 2013 and at 1-min intervals for the rest of the period. Airborne particles were sampled at a height of 4 m above the ground with a flow rate of 5 L min^{-1} using a PM_{10} sampling head (Sven Leckel, Germany). A custom-built Nafion dryer (TROPOS, Leipzig, Germany) was used in the sampling system to keep relative humidity below 40%.

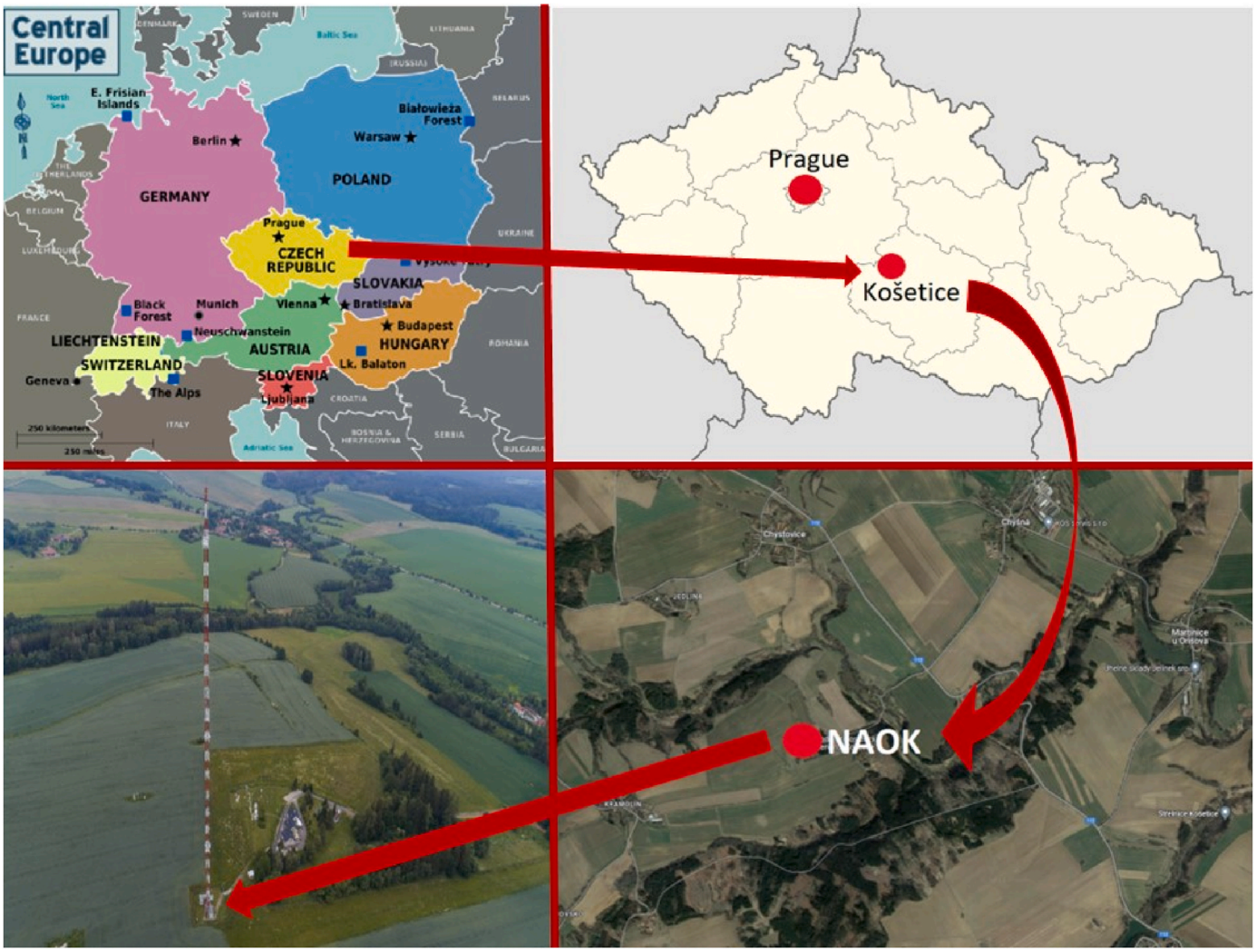

Fig. 1. Location of the national atmospheric observatory Košetice (NAOK).

Full calibration for the instrument was carried out 2–3 times per year (or if needed) using CO_2 as a high-span gas and particle-free air as a low-span gas.

The dataset was processed following the standard monitoring procedure of the European Monitoring and Evaluation Programme (EMEP). The dataset was treated, omitting data from invalid measurements including calibration, malfunctions, extreme and negative values, data above 40% humidity, and data related to agricultural activity in the surrounding field. The data coverage was 56 %. Longer data gaps were observed in spring, autumn and summer 2013, autumn 2017 and autumn and winter 2019. The nephelometer measurements were calculated to the standard *T* and *p* conditions (273.15 K, 1013.25 hPa), corrected for light source non-ideal illumination (Anderson and Ogren, 1998), and used to calculate derived intensive scattering properties such as *SAE_450/700*, *b* and *g*.

2.3. Intensive aerosol optical properties

Unlike σ_{sp} and σ_{bsp}, intensive scattering properties depend on the nature of the aerosol in question, such as size, morphology, and chemical composition (Luoma et al., 2019; Pandolfi et al., 2018; Rajesh and Ramachandran, 2020).

The scattering Ångström exponent (*SAE* 450/700 nm) describes the dependence of aerosol light scattering on wavelength:

$$\mathrm{SAE\_450}\Big/700 = -\frac{\log\left(\sigma_{sp}(450)\right)-\log\left(\sigma_{sp}(700)\right)}{\log(450)-\log(700)} \quad (1)$$

where σ_{sp} (450) and σ_{sp} (700) are the scattering coefficients at wavelengths of light 450 and 700 nm, respectively (Aaltonen et al., 2006; Eck et al., 1999; Müller et al., 2009; Schuster et al., 2006). *SAE* is a dimensionless parameter and depends on particle size distribution (Sierau et al., 2006). *SAE* values < 1 indicate a larger contribution of particles in the coarse mode, whereas *SAE* values near 2 indicate a prevalence of the fine mode (Schuster et al., 2006; Seinfeld and Pandis, 2006).

Although *SAE* describes the wavelength dependence of σ_{sp} and is associated with particle number size distribution, it does not provide sufficient information on the exact share of coarse and fine mode particles in the aerosol multimodal population (Schuster et al., 2006). To obtain more precise information on the ratio of coarse and fine mode particles, Δ*SAE* was calculated using the spectral variation of *SAE* (Perrone et al., 2018):

$$\Delta SAE = SAE\ (450\ \mathrm{nm},\ 550\ \mathrm{nm})\text{-}SAE\ (550\ \mathrm{nm},\ 700\ \mathrm{nm})\ ) \quad (2$$

Negative Δ*SAE* values indicate a dominant single fine particle mode, whereas positive values indicate a more balanced effect of the coarse and fine modes. Δ*SAE* is known to increase with higher contributions of particles in coarse mode (Perrone et al., 2018).

The asymmetry factor (*g*) is one of the key parameters for estimating

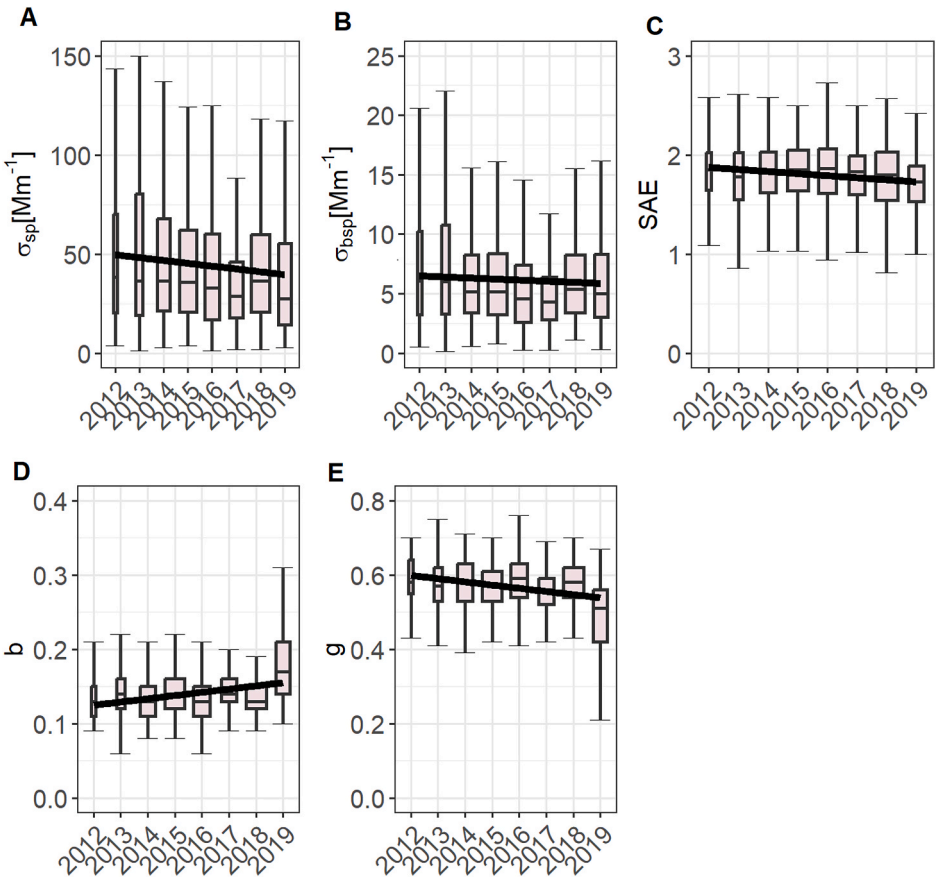

Fig. 2. The interannual variation of A) σ_{sp}, B) σ_{bsp}, C) *SAE_450/700*, D) *b*, and E) *g* at 550 nm. The black lines correspond to the medians of variables, bottom and top sections of the boxes correspond to the 1st and the 3rd quartiles, respectively. The widths of boxplots are proportional to the square roots of number of observations in separate years, and extend to the minimum and maximum values within a range defined by the 1.5 times the interquartile range. Solid line represents trendline.

aerosol radiative transfer (Andrews et al., 2006; Pandolfi et al., 2018; Rama Gopal et al., 2014) and is an essential input for modeling the direct effect of aerosols on climate change. *g* presents the cosine-weighted average of the phase function, describing the probability that the radiation is scattered in a defined direction (Delene and Ogren, 2002; Pandolfi et al., 2018). *g* varies from −1 for complete backscattering to 1 for complete forward scattering. Typically, *g* values range from 0.1 in clean environments to 0.5 for polluted areas, and 0.75 for dust/sea salt particles (Andrews et al., 2006; Wiscombie and Grams, 1976):

$$g = -7.143889 * b_\lambda^3 + 7.464439 * b_\lambda^2 - 3.9356 * b_\lambda + 0.9893 \quad (3)$$

where *b* is the ratio of backscattering to the total scattering coefficient measured at the same wavelength λ (Gopal et al., 2014):

$$b = \frac{\sigma_{bsp}\lambda}{\sigma_{sp}\lambda} \quad (4)$$

The value of *b* characterizes the fraction of light scattered back towards the source of light's origin, ranging from 0 to 1. Larger particles predominantly scatter in a forward direction, resulting in smaller values of *b* (Luoma et al., 2019). Unlike *SAE*, *b* is more sensitive to fine mode particles (Collaud Coen et al., 2007).

2.4. Auxiliary measurements

Additional measurements of carbonaceous aerosol concentrations (Semi-continuous OCEC carbon aerosol analyzer Sunset), SO_2 (UV photometry), NO_X (chemiluminescence), isoprene (gas chromatography), PM_{10} and $PM_{2.5}$ (beta ray absorption), meteorological parameters (temperature, precipitation, cloudiness, and fog events) and aerosol size distribution and concentration (Scanning Mobility Particle Sizer SMPS) were performed at the station alongside TSI 3653 measurement during the whole period. Considering size distribution, the data were divided into three modes: particles under 50 nm as for Aitken mode; particles between 50 and 800 nm as accumulation mode divided into two submodes: from 50 to 200 nm and from 200 to 800 nm, and the whole detectable size range of particles from 10 to 800 nm. In this study, the threshold between fine and coarse mode is 1 μm.

Official meteorological records at NAOK (WMO station number 11628) were used to evaluate the relationship between cloud cover and ASP. The degree of cloud cover was recorded hourly by the meteorological observer in oktas (0/8–8/8) and by automatic measurements from 4 to 5 p.m. UTC and from 9 to 5 a.m. UTC by a Ceilometer CL 51 (Vaisala) placed at the station. The cloudiness categories were Fine (F) for 0 to 2/8, Partly Cloudy (PC) for 3/8 to 5/8, Cloudy (C) for 6/8 and 7/8, and Overcast (O) for 8/8 cloud cover.

A detailed description of these auxiliary measurements can be found in Appendix A.

2.5. Potential source analysis

The variation of the ASP in relation to the wind speed and wind direction was investigated using the conditional bivariate probability function (CBPF) analysis (Uria-Tellaetxe and Carslaw, 2014). The calculation were performed using the openair package (Carslaw and Ropkins, 2012) in R (R Core Team, 2020; R Core Team, 2020) and the 75th percentile was used as a threshold, i.e., the probability of the ASP between the 75th and 100th percentiles was calculated for different years and months.

To study the location of potential sources of light scattering particles,

Table 1
The result of Mann Kendall Seasonal trend test including p, tau, Kendall score S and variance of S. The p value below 0.05 indicates significant trend.

ASP	p	tau	Kendall score S	Variance of S
σ_{sp} 450	0.021	−0.175	−554	57,933
σ_{sp} 550	0.037	−0.159	−502	57,933
σ_{sp} 700	0.058	−0.144	−456	57,933
σ_{bsp} 450	0.406	−0.063	−200	57,933
σ_{bsp} 550	0.260	−0.086	−271	57,928
σ_{bsp} 700	0.823	−0.017	−54	57,931
*SAE*_450/700	0.135	−0.115	−360	57,889
ΔSAE	0.243	0.090	281	57,850
b 450	0.062	0.151	443	56,296
b 550	0.102	0.131	390	56,769
b 700	0.006	0.218	655	57,027
g 450	0.054	−0.150	−462	57,615
g 550	0.049	−0.153	−472	57,617
g 700	0.006	−0.214	−661	57,663

air mass back trajectories were calculated using the HYSPLIT_4 model (Draxler, 1998; NOAA Air Resources Laboratory, 2023; Rolph et al., 2017; Stein et al., 2015), as well as a Potential Source Contribution Function Analysis (PSCF) being performed.

NCEP/NCAR Reanalysis 1 meteorological data (Kalnay et al., 1996) were used to calculate 72-h air mass backward trajectories arriving at 200 m a.g.l. every 3 h. The PSCF analysis was accomplished using the same back trajectories to determine the probability of source contributions from specific geographical locations impacting the receptor site. The source location is defined by latitudinal (i) and longitudinal (j) coordinates (Ashbaugh et al., 1985):

$$PSCF = \frac{m_{i,j}}{n_{i,j}}, \quad (5)$$

where $m_{i,j}$ represents how many times the concentration exceeds the predefined limit (75th percentile), and $n_{i,j}$ the number of times the trajectories' endpoints enter the *i,j*th lat-long grid cell. PSCF values range from 0 to 1, with values close to 1 indicating a probable source location. The study domain extends from 20° W to 40° E and from 30° N to 70° N, split into 1° × 1° cells (2205 total cells). A weighting function $W_{i,j}$ was used to restrain the contribution from cells with fewer trajectory hits ($n_{i,j}$) than three times the mean value of endpoints $\bar{n}$, i.e., 680 in this work (Zíková et al., 2016):

$$W_{i,j} = \begin{cases} 1.00 & n_{i,j} \geq 2\,\bar{n} \\ 0.75 & 2\,\bar{n} > n_{i,j} \geq \bar{n} \\ 0.50 & \bar{n} > n_{i,j} \geq 0.5\,\bar{n} \\ 0.15 & 0.5\,\bar{n} > n_{i,j} \end{cases} \quad (6)$$

3. Results and discussion

3.1. The annual variation of light scattering properties

The median σ_{sp} measured at 550 nm for the whole observed period was 35.20 Mm^{-1}, with annual median values varying from 45.90 Mm^{-1} in 2012 to 28.50 Mm^{-1} in 2019 (Fig. 2A, Table S.2 and S.3).

The overall median of σ_{bsp} at 550 nm was 5.07 Mm^{-1}, annual medians ranging from 6.26 Mm^{-1} in 2013 to 4.30 Mm^{-1} in 2017 (Fig. 2B, Table S.2 and S.3).

The interannual changes of all ASP were tested for monotonic trend with the Mann–Kendall Seasonal test. Only σ_{sp} trends at 450 and 550 nm were statistically significant, no σ_{bsp} showed significant decrease. Significant decrease of values was *g* at 550 and 700 nm, whereas a significant increase in values was observed for *b* at 700 nm ($\alpha = 0.05$, $p < 0.05$, Table 1).

σ_{sp} and σ_{bsp} at 550 nm decreased by 2.05 Mm^{-1}/year (−4.45 % per year) and 0.099 Mm^{-1}/year (−1.63% per year), respectively. The decrease in σ_{sp} and σ_{bsp} with increasing wavelength (from 450 to 700 nm) in this study may indicate the presence of both coarse and fine mode particles with fine particles still dominating. The aerosol light scattering is dependent on particle size and decreases when particle size exceeds the wavelength of incident light (Perrone et al., 2016, 2018).

Table 2
Spearman correlation coefficients between ASP at 550 nm and physical properties of particles (number concentration, mass, volume and area) for different size modes. All coefficients are significant at $p < 0.0001$.

Spearman coefficient	Num. conc. 10–800 nm	Num. conc. 200–800 nm	Num. conc. 50–200 nm	Num. conc. <50 nm
σ_{sp}	0.12	0.85	0.37	−0.25
σ_{bsp}	0.19	0.86	0.45	−0.20
SAE_450/700	0.07	0.04	0.12	0.04
ΔSAE	0.20	−0.53	−0.04	0.44
b	0.22	−0.50	0.06	0.39
g	−0.22	0.61	−0.07	−0.40

Spearman coefficient	Particle volume 10–800 nm	Particle volume 200–800 nm	Particle volume 50–200 nm	Particle volume <50 nm
σ_{sp}	0.88	0.90	0.53	−0.14
σ_{bsp}	0.89	0.89	0.61	−0.08
SAE_450/700	−0.07	−0.10	0.15	0.07
ΔSAE	−0.55	−0.60	−0.18	0.33
b	−0.57	−0.65	−0.04	0.34
g	0.57	0.66	0.04	−0.35

Spearman coefficient	Particle mass 10–800 nm	Particle mass 200–800 nm	Particle mass 50–200 nm	Particle mass <50 nm
σ_{sp}	0.88	0.90	0.53	−0.14
σ_{bsp}	0.89	0.89	0.61	−0.09
SAE_450/700	−0.07	−0.10	0.15	0.07
ΔSAE	−0.55	−0.60	−0.18	0.34
b	−0.57	−0.65	−0.04	0.35
g	0.57	0.66	0.04	−0.35

Spearman coefficient	Particle area 10–800 nm	Particle area 200–800 nm	Particle area 50–200 nm	Particle area <50 nm
σ_{sp}	0.79	0.89	0.49	−0.18
σ_{bsp}	0.83	0.89	0.57	−0.12
SAE_450/700	0.01	−0.05	0.14	0.06
ΔSAE	−0.43	−0.58	−0.13	0.37
b	−0.40	−0.61	−0.01	0.37
g	0.40	0.61	0.01	−0.37

Correlation coefficients between number concentration in individual modes and selected light scattering properties are shown in Table 2.

σ_{sp} and σ_{bsp} showed the strongest positive correlations with the particle number concentration from 200 to 800 nm ($R = 0.85$ and 0.86, respectively), weaker positive correlations were found from 50 to 200 nm ($R = 0.37$ and 0.45, respectively) and negative correlations were found in the particle mode smaller than 50 nm ($R = -0.25$ and −0.20, respectively). This suggests that particles in the accumulation mode (200–800 nm) are the main contributors to aerosol light scattering (Hinds, 1999; Seinfeld and Pandis, 2006). The widest size particle mode from 10 to 800 nm showed weak correlation ($R = 0.12$ for σ_{sp} and $R = 0.19$ for σ_{bsp} at 550 nm) (Table 2).

The median σ_{sp} value observed in this study is comparable to those previously presented by Pandolfi et al. (2018) at rural sites in Europe, e.g. 32.36 Mm^{-1} and 33.17 Mm^{-1} at NAOK and Melpitz, respectively (Table 3).

Higher median values of σ_{sp} at 550 nm (>45 Mm^{-1}) were measured at other rural and urban sites due to the influence of road traffic and industrial activities (Pandolfi et al., 2018; Titos et al., 2012). Low median values of σ_{sp} at 550 nm were reported in Pandolfi et al. (2018) at remote stations Zeppelin in Norway (2.82 Mm^{-1}), Pallas in Finland (4.29 Mm^{-1}), Troll in Antarctica (0.72 Mm^{-1}) and at mountain stations

Table 3
Median values of selected ASP measured at 550 nm at NAOK and other European sites.

Station	σ_{sp} (Mm^{-1})	*SAE* (450/700)	*b*	*g*	Type	Period	Ref.
Košetice (Czech Rep.)	35.20	1.82	0.140	0.570	rural	2012–2019	This study
Košetice (Czech Rep.)	32.26	1.82	0.140	0.560	rural	2013–2015	Pandolfi et al. (2018)
Melpitz (Germany)	33.17	1.82	0.148	0.543	rural	2007–2015	
Ispra (Italy)	56.12	2.02	0.135	0.572	rural	2004–2014	
K-Puszta (Hungary)	48.99	2.05	0.130	0.585	rural	2006–2014	
Demokritos Athens (Greece)	47.39	1.7	0.105	0.649	urban	2012–2015	
Capo Granitola (Italy)	33.07	1.17	0.100	0.660	coastal	2015–2018	Donateo et al. (2020)
Lamezia Terme (Italy)	30.42	2.13	0.110	0.630	coastal	2015–2018	
Lecce (Italy)	39.83	1.84	0.080	0.710	urban	2015–2018	
Granada (Spain)	55	1.7	–	–	urban	2006–2007	Titos et al. (2012)

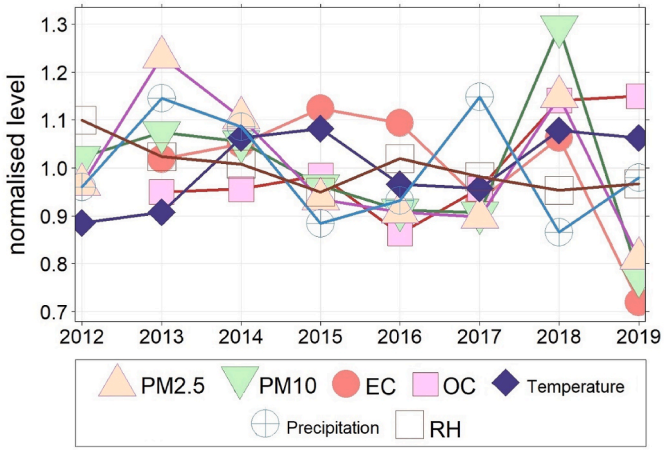

Fig. 3. Interannual variations of $PM_{2.5}$, PM_{10}, EC, OC and meteorological parameters (temperature and precipitation). Each dataset is divided by its means to compare variables with diverse ranges and units; y axis is dimensionless.

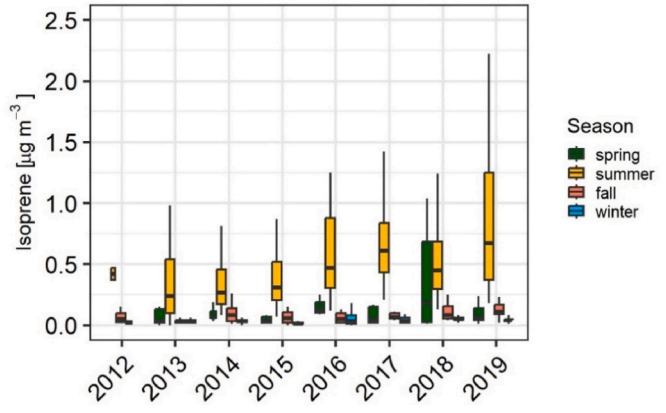

Fig. 4. The interannual and seasonal evolution of isoprene concentration (2012–2019) at NAOK. Black line represents the median, whiskers extend to the minimum and maximum values within a range defined by the 1.5 times the interquartile range.

Izaña in Spain (7.32 Mm^{-1}), Jungfraujoch in Switzerland (2.41 Mm^{-1}), and Mt Chacaltaya in Bolivia (4.94 Mm^{-1}). The observed decrease of σ_{sp} and σ_{bsp} may suggest the effectiveness of air pollution policies already in place such as European Ambient Air Quality 2008/50/EC (The European Parliament, The Council of the European union, 2008) observed across Europe (Cherian et al., 2014; Colette et al., 2011; Koolen and Rothenberg, 2019; Quaas et al., 2020; Wang et al., 2020). This is consistent with the sharp decline in EC concentration over the years (Fig. 3 and Table S.5).

Higher median values of σ_{sp} and σ_{bsp} in 2018 were correlated with increased concentrations in PM_{10}, $PM_{2.5}$, and carbonaceous aerosols, especially organic carbon (OC, Figure S.5), increased temperature and lower precipitation rate. This could be explained by the increased mean temperatures and lower precipitation and RH also recorded at NAOK in 2018 (Fig. 3 and Table S.5).

Šmejkalová and Brzezina (2022) analyzed the effect of drought on PM concentrations at various meteorological stations in the Czech Republic, including NAOK. They found 138.3 % higher PM_{10} concentrations during dry periods, mainly due to extent of resuspension and soil erosion caused by low soil moisture. As ASP could be influenced by the formation of secondary organic aerosols (SOA), the interannual trend of the most common SOA precursor, isoprene, was also examined at NAOK (Fig. 4). The annual median concentration of isoprene ranged from 0.034 $\mu g/m^3$ in 2012 to 0.108 $\mu g/m^3$ in 2018, which is consistent with the significant increase in OC concentrations observed in 2018 (Figure S.5).

The annual median *SAE*_450/700 value was the highest in 2016 (1.86) and the lowest in 2019 (1.73). The *SAE* values close to 2 indicate that the aerosol population collected at the rural site is dominated by fine particles. Similar median values of *SAE*_450/700 for the whole measurement period, 1.82, were previously reported at NAOK and at Melpitz (a rural site in Germany) by Pandolfi et al. (2018). A decreasing *SAE_450/700* (0.021/year) was observed over the measurement period, which indicates a relative shift towards larger particle sizes, possibly due to aerosol aging in the atmosphere. Due to the changes in *SAE_450/700*, long-range transport might have gotten to be a more significant source of aged aerosol particles at NAOK (see Chapter 3.5 Source apportionment). This is consistent with the obtained *ΔSAE* values, with annual median values ranging from −0.20 in 2012 to 0.16 in 2019. Although the trend of *ΔSAE* is not statistically significant (Mann Kendall Seasonal test, $\alpha = 0.05$, $p < 0.05$), the increasing potential of *ΔSAE* suggests a future shift of particle size towards the accumulation mode over the study period and a need of future observation.

However, the negative overall median *ΔSAE* (−0.03) suggests that the aerosol size distribution remained dominated by fine particles which scatter light backwards more efficiently compared to larger size modes. This also agrees with the increasing *b* median values (Fig. 2D), ranging from 0.13 in 2012 to 0.17 in 2019 (0.004/year). The annual median *b* was 0.14, in agreement with that observed and reported in Pandolfi et al. (2018). *b* also increased with wavelength (from 450 to 70 nm), suggesting the dominance of the fine particle mode on backscatter (Table S.2 and S.3) (Perrone et al., 2018). Similar conclusions can be drawn from the changes in *g* at 550 nm, shifting to smaller values over time (Fig. 2E). Although the trend of *g* is decreasing and aerosol particles have become more effective in scattering the incident light in the backward direction, forward scattering is still the predominant scattering direction at NAOK.

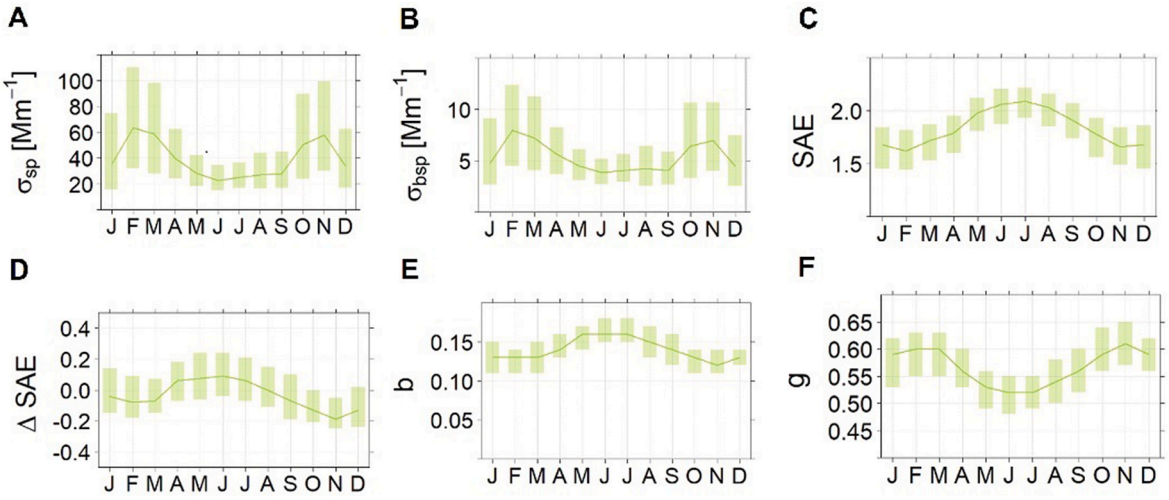

Fig. 5. The monthly variation of A) σ_{sp}, B) σ_{bsp}, C) *SAE_450/700*, D) Δ*SAE*, E) *b* and F) *g*. All variables are shown for 550 nm. The figures show median variations between 25th and 75th percentiles.

3.2. The seasonal and monthly variation of light scattering properties

Seasonal and monthly variations of selected ASP at 550 nm were also examined (Table S.6). In this study, spring, summer, autumn and winter seasons consist of March + April + May, June + July + August, September + October + November and January + February + December, respectively. The highest seasonal medians of σ_{sp} (Fig. 5A) were observed during the winter (44.67 Mm^{-1}) and autumn (46.83 Mm^{-1}), with generally large variability. The lowest seasonal median of σ_{sp} was observed in the summer (25.37 Mm^{-1}).

The same pattern was observed for σ_{bsp} (Fig. 5B). The highest values of both σ_{sp} (≥58.0 Mm^{-1}) and σ_{bsp} (≥7.0 Mm^{-1}) were measured in February, March, and November. Aerosol light scattering could be influenced by chemical composition, mainly inorganic salts (sea salts, nitrates, sulfates), minerals, organic matter, etc. In this study, we used the concentrations of SO_2 and NO_X as precursors of sulfate and nitrate salts (Figure S.1).

SO_2 and NO_X, as well as OC and EC (Figure S.2), showed similar behavior as σ_{sp} and σ_{bsp}, with the highest values being observed in winter.

This could be attributed to enhanced emissions from combustion sources (residential heating) during this season, and favorable meteorological conditions for the accumulation of particles (higher atmospheric stability), which led to a lower dilution rate (Kalmus et al., 2022; Kim, 2022; Seinfeld and Pandis, 2006).

In contrast, *SAE_450/700* showed the highest seasonal median in summer (2.05) and the lowest seasonal median in winter and autumn (1.64 and 1.66, respectively). *SAE_450/700* reached its highest monthly median in July (2.09), and its lowest monthly median in February (1.62, Fig. 5C). A similar seasonal pattern was observed for Δ*SAE* and *b* reaching their maximum medians in summer (Fig. 5D and E). The lower values of Δ*SAE* and *b* in the colder season suggest a higher fraction of aerosols in the higher end of accumulation mode in winter (Figure S.6) (Luoma et al., 2019). The lower *b* and higher *g* in winter (Fig. 5E and F) suggest that this aerosol population scatters light considerably in the forward direction. Conversely, the higher values of Δ*SAE* and *b* in summer suggest a non-negligible fraction of accumulation mode particles on the lower size end, possibly attributed to the increased formation of SOA (Luoma et al., 2019). The higher concentration of isoprene observed in summer could promote SOC formation (Fig. 4 and S.2) with a higher backscattering fraction, as may be suggested by the lower *g* observed during this season (seasonal median 0.53). The analysis of

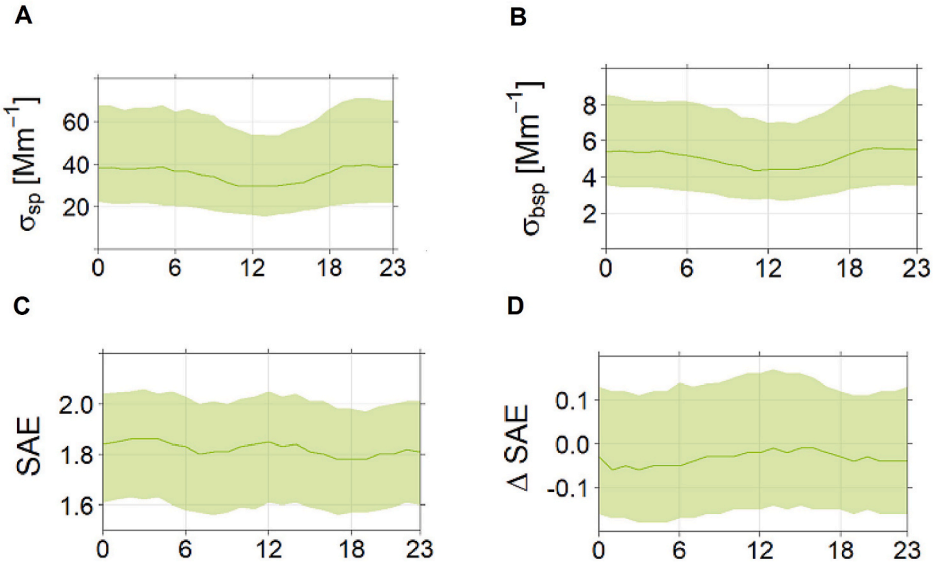

Fig. 6. The diurnal variation of A) σ_{sp}, B) σ_{bsp}, C) *SAE_450/700* and D) Δ*SAE* at 550 nm (in UTC) showing the median with 25th and 75th percentiles (shaded).

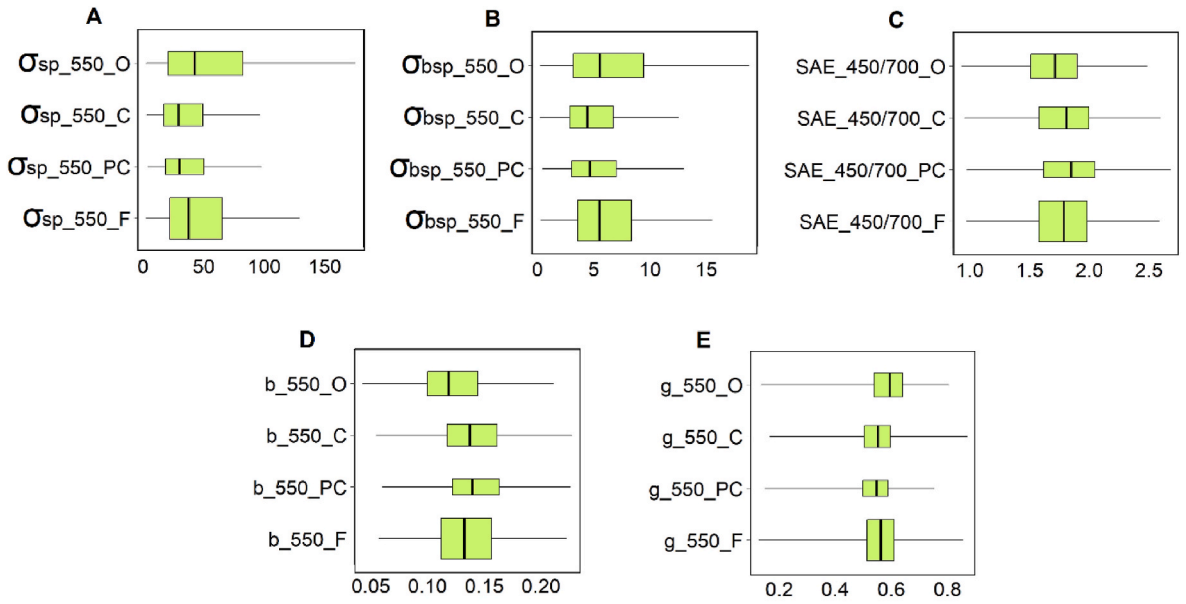

Fig. 7. A) σ_{sp} [Mm^{-1}], B) σ_{bsp} [Mm^{-1}], C) *SAE_450/700*, D) *b*, E) *g* during different meteorological conditions where O = overcast, C = cloudy, PC = partly cloudy and F = fine at 550 nm. Black line represents median, colored areas the 25th and 75th intervals, the whiskers extend to the minimum and maximum values within a range defined by the 1.5 times the interquartile range. The widths of boxplots are proportional to the square roots of number of observations in cloud categories.

Spearman correlation coefficient between σ_{bsp} at 550 nm and SOC concentration showed the highest values in summer (R = 0.40) compared to other seasons. Also, SOC and isoprene showed a highest correlation in summer (R = 0.51) which may suggest that isoprene, among other factors, contributed to SOC formation and to the higher backscatter fraction in summer.

ΔSAE, *b* and *g* showed stronger relations with particle mass, volume, and area in the 200–800 nm mode (R ~ −0.61, −0.65 and 0.66, respectively) than in the other observed modes (under 200 nm). This implies that the variation in *ΔSAE*, *b* and *g* is the most sensitive to the changes in the accumulation mode particle concentration (M. Collaud Coen et al., 2007; Delene and Ogren, 2002).

3.3. The weekly and diurnal variations of light scattering properties

The difference between days of the week as well as between hours of the day was tested using a non-parametric pairwise Wilcoxon Rank Sum Test ($\alpha = 0.05$, $p < 0.05$) using the Holm method. A weak weekly cycle was found for σ_{sp} and σ_{bsp} at 550 nm with a minimum on Monday (Table S.7) and significantly higher levels from Wednesday to Saturday ($\alpha = 0.05$, $p < 0.05$), which in turn decreased once again on Sunday. σ_{sp} was 10.14% lower on average during Monday and Sunday compared to the rest of week. The relative decrease in concentrations during the weekend suggests reduced anthropogenic emissions during weekends. Concerning *SAE_450/700*, slightly lower values were found in the middle of the week and higher values during the weekend (maximum on Sunday). No differences in weekly variation were found for separate seasons. The highest *ΔSAE* median value (−0.01) was found on Monday, and the lowest value (−0.05) on Friday and Saturday. Higher *SAE_450/700* and lower *ΔSAE* observed during the weekend could be due to an accumulation of fine particles (having longer lifetimes) emitted during the working day, which could stay in the atmosphere for prolonged time during the weekend, especially on Saturday, as previously observed by Mbengue et al. (2018).

Table 4
Comparison of obtained results with Gopal et al. (2014).

Mean values at 550 nm	Meteo	This study	Gopal et al. (2014)
σ_{sp} [Mm^{-1}]	Clear/F day	49.29	90
	Cloudy/O day	56.98	40
σ_{bsp} [Mm^{-1}]	Clear/F day	6.54	17
	Cloudy/O day	6.82	5
SAE_450/700	Clear/F day	1.80	1.4
	Cloudy/O day	1.74	0.6

The daily median variations of σ_{sp} and σ_{bsp} followed the same pattern across the whole week with higher levels observed during nighttime and early morning (Fig. 6A and B, Table S.8), significantly lower values from 9 a.m. to 5 p.m. ($\alpha = 0.05$, $p < 0.05$) with a minimum daily median observed around 1 p.m. (29.71 and 4.38 Mm^{-1}, respectively) and another maximum daily median at 9 p.m. (39.58 and 5.55 Mm^{-1}, respectively). These higher levels during the nighttime could be caused by the lower planetary boundary layer which suppresses dilution of the aerosol.

The diurnal variation of *SAE_450/700* (Fig. 6C) showed two maximum daily medians: one of 1.86 from the nighttime to early morning (2–4 a.m.), and a second with a value of 1.85 around noon (12 a.m.). *ΔSAE* showed the highest median value (−0.01) between 1 and 4 p.m. and the lowest value (−0.06) during nighttime (Fig. 6D).

Increased *SAE_450/700* associated with decreased *ΔSAE* during night hours indicate the presence of particles in the higher end accumulation mode (200–800 nm) and coarse mode, likely due to the poor atmospheric dilution conditions (favorable for aerosol accumulation), whereas the increase in both *SAE_450/700* and *ΔSAE* at noon suggests new particle formation (Luoma et al., 2019). These results are consistent with the increasing *b* with wavelength throughout the week and day, indicating the dominance of fine mode in the aerosol population. No statistically significant trend was observed for *b* and *g*.

3.4. Influence of meteorological characteristics on ASP

3.4.1. ASP during differing cloud cover

During the measured period, fine (F) days dominated (54.79%), followed by overcast (O) days (19.48%), cloudy (C) days (16.46%) and partly cloudy (PC) days (8.76%). For the remaining 0.51% days, either no measurement was recorded, or an error had occurred. Significant difference ($p < 0.05$) was observed in σ_{sp}, σ_{bsp}, *b* and *g* between the O and F days compared to C and PC days at all wavelengths (Fig. 7, Table S.10).

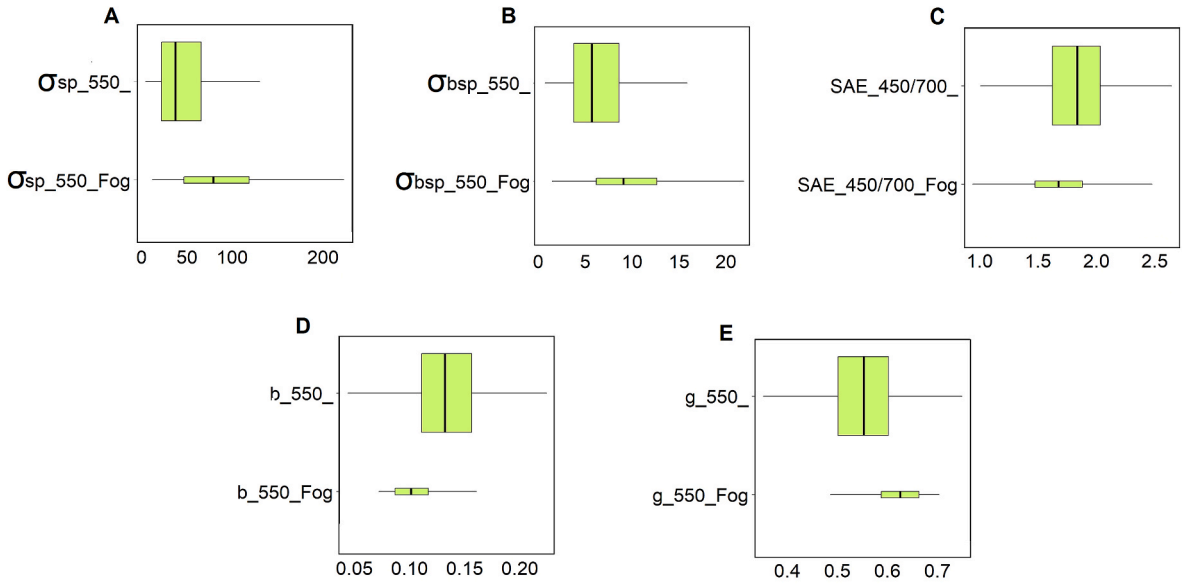

Fig. 8. Comparison of A) σ_{sp} (Mm^{-1}), B) σ_{bsp} (Mm^{-1}), C) *SAE_450/700*, D) *b*, E) *g* during days with (Fog) and without (missing parameter) fog event at 450 nm (blue), 550 nm (green), 700 nm (red) wavelength. Black line represents the median, colored areas the 25th and 75th intervals, the whiskers extend to the minimum and maximum values within a range defined by the 1.5 times the interquartile range. The widths of boxplots are proportional to the square roots of number of observations.

σ_{sp}, σ_{bsp}, and g were higher during O and F days compared to C and PC, whereas *SAE_450/700* and *b* showed opposite behavior. No difference was found between C and PC days for almost all variables ($p > 0.05$).

Several recent papers discussed the impact of cloudiness on the aerosol-radiation relationship, highlighting the limitations of solely studying clear-sky aerosol light scattering (Ghan, 2013; Li et al., 2022; Myhre et al., 2020; Ogren et al., 2009; Thornhill et al., 2021). Gopal et al. (2014) showed a decrease in σ_{sp} during cloudy days compared to hazy and clear days, attributed to the aerosol washout effect through precipitation. Although our categorization criteria were slightly different, we classified clear conditions as F days and cloudy conditions as O days to allow for comparisons with other studies (Table 4).

Higher average values of σ_{sp} and σ_{bsp} observed during F days in India may be attributed to higher population density and worsened air pollution. In this study, higher values were found during O days compared to F days (Fig. 7A and B). The higher scattering properties during the O days at NAOK could be explained by altered hygroscopic properties of the aerosols due to higher RH during O days. Although we followed the WMO/GAW standard monitoring guidelines and kept samples under 40% RH, the heterogenous reactions with RH in the atmosphere could affect the particle composition, mixing state of particles or morphology, resulting in a higher aerosol light scattering at NAOK. Another possible explanation is an effect of cloud processing. Isokääntä et al. (2022) observed increased concentration of particles in the accumulation mode in the aerosol population which had been in-cloud compared to the fine sky air (no rain or clouds during the last 24 h). Moreover, Noble and Hudson (2019) reported higher concentrations and greater mean particle diameters of accumulation mode particles in the presence of greater cloud cover. The greater sizes but lower concentrations were observed also for Aitken mode during greater cloud cover with successive hours of a cloud cover supporting the production of accumulation mode particles. On the other hand, hours of clear sky resulted in the decrease of the total mean particle diameters, increase of Aitken mode concentration while accumulation mode concentration remained stable.

The analysis of *SAE_450/700* for different categories of cloudiness revealed significant differences between the categories, except for C and F days (Fig. 7C). *SAE_450/700* was smallest during O days, indicating the presence of larger particles, similar to Gopal et al. (2014). The lower planetary boundary layer during O days could accelerate the condensation of vapors onto particles, leading to enhanced size growth.

The observed behavior for *g* was similar to that of σ_{sp} and σ_{bsp} (Fig. 7E), with significantly higher values for O days compared to F, PC and C days. The lower values during F, C and PC days suggest a relatively larger portion of backscattering to total light scattering.

3.4.2. ASP during fog events

All selected ASP were significantly different during days with fog (visibility up to 1 km) compared to the no-fog days (Fig. 8). Fog events were presented only in 0.86 % of the observed period. Median values of σ_{sp} and σ_{bsp} at 550 nm were higher during fog events (76.71 and 8.57 Mm^{-1}, respectively) compared to non-fog events (34.82 and 5.21 Mm^{-1}, respectively), and doubled to values across any cloudiness type (Fig. 8A and B). Fog events favor the condensation of water vapor on pre-existing particles and stimulate particle growth indicated by decreasing *SAE_450/700* (Fig. 8C). Accumulation and droplet mode particles are more present during fog events due to the particle growth, and due to the fact that they are effective in terms of aerosol light extinction, σ_{sp} and σ_{bsp} were observed higher during fog events than during the non-fog events (Elias et al., 2009).

Significant increases in σ_{sp} and σ_{bsp} during fog and hazy days have also been presented in other studies (Qin et al., 2018; Safai et al., 2019; Ganguly et al., 2006; Tiwari et al., 2015). Here, *SAE_450/700* median during fog events was 1.67, which corresponds to the values during O days. In contrast, a higher *SAE_450/700* median of 1.83 was observed during non-fog events, similar to F days.

Median *b* values were significantly lower during fog events, 0.11, compared to 0.15 during no-fog events (Fig. 8D), indicating decreased backscattering fraction of total scattered light during fog. The fog *b* value is even lower than on any of the cloud-categorized days, also possibly due to multiple scattering.

Due to the high concentration of droplets and particles in fog, any scattered beam could be later scattered on another particle, decreasing the energy of the latter-scattered beam, leading to the disappearance of the backscattered signal below the limit of detection. Another possible explanation is the shift in size due to the growth of particles and the narrowing of the number size distribution of particles (Zíková and

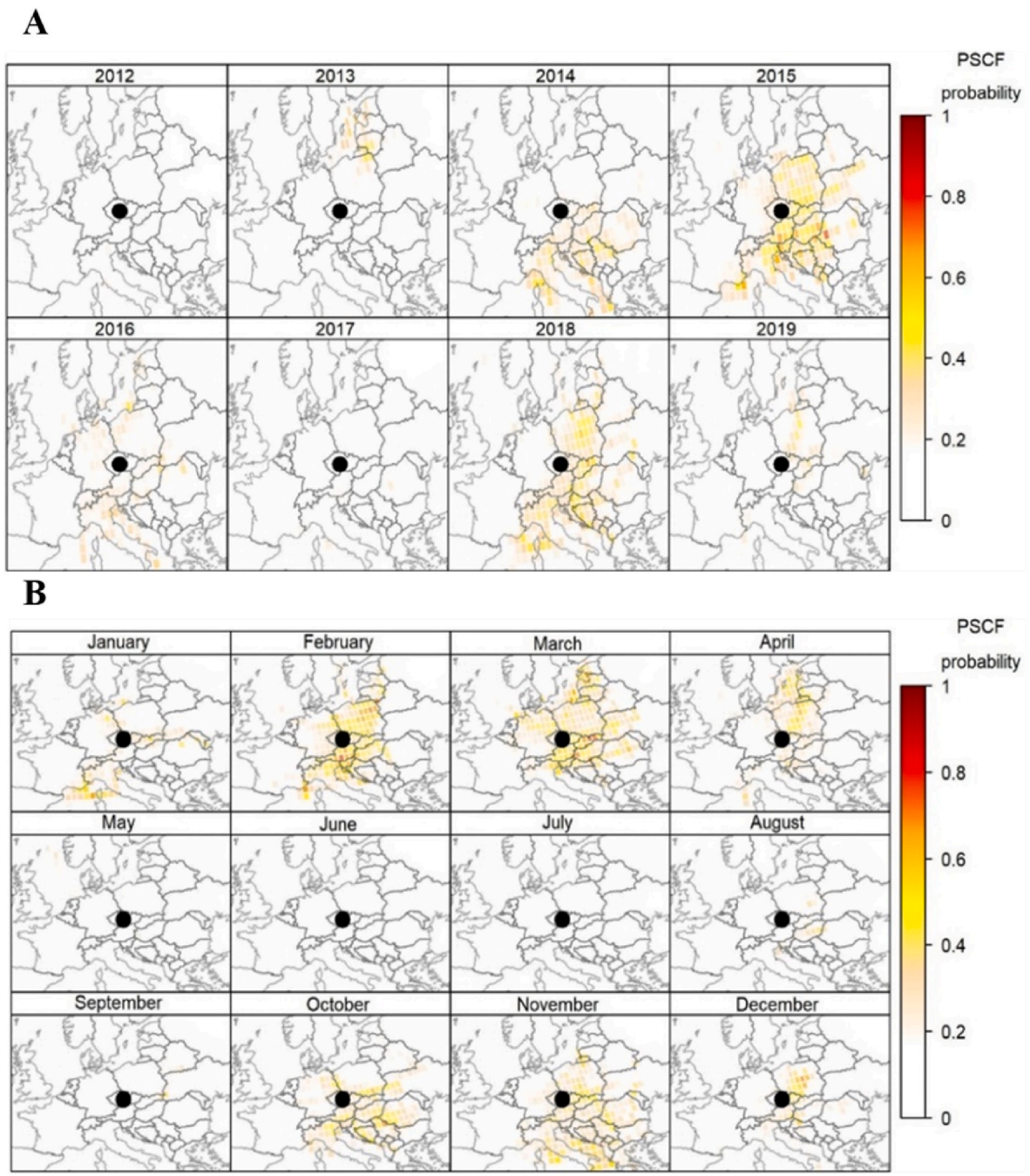

Fig. 9. PSCF of particle sources with a σ_{sp} at 550 nm calculated A) annually and B) monthly (average throughout the observed period). The black circle denotes the location of NAOK. The set point for calculation is the 75th percentile.

Ždímal, 2016).

Forward scattering prevalence was also found during the fog event, with *g* values of 0.63 at 550 nm compared to 0.55 for the non-fog event (Fig. 8E). This is consistent with previous analyses that indicated a significant difference in ASP during fog events. Zhang et al. (2020) also noticed the decrease in *SAE_450/700* and *b* as well as the increase in *g* when fog events are presented.

3.5. Source apportionment

The CBPF and PSCF were calculated for σ_{sp} for different months and years (Fig. 9). The higher levels of σ_{sp} were observed mostly under moderate (5–8 m s^{-1}) to strong (8–12 ms^{-1}) wind speed from the SE in 2012 and 2015, and under strong wind from the N and NE in 2013 (Figure S.7 A). There was no clear wind speed-direction dependence observed for other years. For the PSCF, the highest probability of σ_{sp} source locations (Czech Republic, Poland, Austria, Hungary, Northern-East and Southern Europe) were observed in 2015 and 2018 (Fig. 9A), during which higher concentrations of carbonaceous aerosols, PM_{10}, and $PM_{2.5}$ were observed (Fig. 3). No clear source location was identified by the PSCF for the other years, likely due to the use of the overall annual 75th percentile as the limit value. Therefore, the higher probability of source identification in 2015 and 2018 could be caused by meteorological conditions (warmer atmosphere and lower precipitation rate) and the increased SOA formation observed during these years.

During the measurement period, the highest values of σ_{sp} were found in the cold months (Fig. 9B) associated with low wind speed conditions around the receptor site, and under moderate to stronger wind from N,

NE and SE (Figure S.7 B). The PSCF identified well-distributed source locations associated with continental air masses in Central Europe, with stronger signals observed in late winter and early spring in the Czech Republic, neighboring countries, and the Baltics. In autumn, some sources were also located in the Balkans and the Mediterranean Sea. Despite the increased probability identified for some years and months, probabilities did not exceed 0.5 for the majority of grid points.

Also, the source location was well spatially distributed without any significant contribution from local sources. The identified source locations may thus more closely reflect the synoptic situation over Europe and well-distributed sources than well-defined sources of pollution. This further confirms that the NAOK station is suitable for the rural background observation of aerosol light scattering to reliably record the changing trends across the European continent.

4. Summary and conclusion

This study characterized the light scattering properties of aerosols at a Central European background site from 2012 to 2019. The total scattering coefficient σ_{sp} and back scattering coefficient σ_{bsp} were measured by the integrated nephelometer TSI 3653 at three wavelengths (450, 500 and 700 nm). Additional climate-relevant variables such as scattering Ångström exponent *SAE_450/700* and its wavelength dependence Δ*SAE*, the hemispheric backscattering ratio *b* and the asymmetry factor *g* were also calculated.

σ_{sp} at 450 nm decreased by 4.56 % per year and σ_{sp} at 550 nm decreased by 4.45 % per year while overall medians were 51.17 Mm^{-1} and 35.20 Mm^{-1}, respectively. The decreasing trend of σ_{sp} was disrupted by increased median in 2018 due to higher temperatures, less precipitation rate, increased PM_{10} and $PM_{2.5}$ concentrations and the presence of carbonaceous aerosols. No significant decrease was observed for σ_{bsp}. The *SAE_450/700* value was close to 2 during the observed period, and decreased over time, implying a relative shift of the particles to larger accumulation mode sizes. The increase in *b* and decrease in *g* over the years suggest a higher portion of scattered light is being scattered back to the upper hemisphere. In addition to size, this could also be explained by potential changes in aerosol chemical composition.

The highest levels of σ_{sp} and σ_{bsp} were observed in cold seasons, mainly due to local residential heating, (biomass and fossil fuels burning), lower height of the planetary boundary layer and a more stable atmosphere. In summer, elevated *SAE_450/700* (seasonal median 2.04) indicates increased SOA formation, whereas in winter (seasonal median 1.66), the particles may participate in heterogeneous reactions and aerosol ageing due to longer lifetimes, resulting in their larger sizes. Increased *b* in summer supports a hypothesis of the presence of backscattering aerosol species, e.g., SOA, in higher concentrations.

The diurnal variation of σ_{sp} and σ_{bsp} was mainly affected by planetary boundary layer height and anthropogenic activities. Diurnal variations of *SAE_450/700* and Δ*SAE* suggest the prevalence of fine particles in the larger accumulation mode during the night (from poor atmospheric dilution conditions and the condensation of aerosols) and in the smaller accumulation mode at noon (new particle formation). Higher levels of σ_{sp} and σ_{bsp} were observed during the overcast (O) days, compared to fine (F) cloudy (C) or partly cloudy (PC) days ($p < 0.05$). During O days, enhanced size growth of particles could lead to lower *SAE_450/700* values, while a lower backscattering ratios were also observed. During fog events, particle growth could be more induced due to condensation of water vapor on pre-existing particles, leading to even higher σ_{sp} and σ_{bsp} medians at 550 nm (76.71 Mm^{-1} and 8.57 Mm^{-1}, respectively) compared to no-fog events (34.82 Mm^{-1} and 5.21 Mm^{-1}, respectively).

The ASP showed the strongest correlation with the number, mass, area and volume of particles in the size range from 200 to 800 nm, close to the wavelength of visible light.

The source apportionment of σ_{sp} at NAOK showed well distributed sources location mainly associated with continental air masses over Central European region. This study shows that the NAOK could be considered as a regional background site representative to provide reliable observation of the temporal trend of aerosol optical properties across the European continent.

CRediT authorship contribution statement

Lenka Suchánková: Conceptualization, Data curation, Formal analysis, Investigation, Methodology, Validation, Visualization, Writing – original draft, Writing – review & editing. **Saliou Mbengue:** Data curation, Formal analysis, Methodology, Supervision, Writing – review & editing. **Naděžda Zíková:** Formal analysis, Investigation, Resources, Visualization. **Adéla Holubová Šmejkalová:** Data curation, Formal analysis, Investigation, Resources. **Roman Prokeš:** Funding acquisition, Project administration, Supervision. **Ivan Holoubek:** Funding acquisition, Project administration, Supervision. **Vladimír Ždímal:** Funding acquisition, Investigation, Methodology, Project administration, Writing – review & editing.

Declaration of competing interest

The authors declare that they have no known competing financial interests or personal relationships that could have appeared to influence the work reported in this paper.

Data availability

Data will be made available on request.

Acknowledgements

This work was financially supported by the Ministry of Education, Youth and Sports of CR within the Large Research Infrastructure ACTRIS Czech Republic (LM2023030] and the CzeCOS (LM2023048). Authors thank to the Czech Science Foundation (GJ18-15065Y) and Laurence Windell for the English proof reading. RP thanks the RECETOX RI (No LM2023069) and the OP RDE project (the CETOCOEN EXCELLENCE No. CZ.02.1.01/0.0/0.0/17_043/0009632) for supportive background. This work was supported from the European Union's Horizon 2020 research and innovation program under grant agreement No 857560. This publication reflects only the author's view, and the European Commission is not responsible for any use that may be made of the information it contains.

Appendix A. Supplementary data

Supplementary data to this article can be found online at https://doi.org/10.1016/j.atmosenv.2023.120292.

References

Aaltonen, V., Lihavainen, H., Kerminen, V.-M., Komppula, M., Hatakka, J., Enroth, J., Kulmala, M., Viisanen, Y., 2006. Measurements of optical properties of atmospheric aerosols in Northern Finland. Atmos. Chem. Phys. 9, 1155–1164. https://doi.org/10.5194/acp-6-1155-2006.

Anderson, Theodore L., Ogren, J.A., 1998. Determining aerosol radiative properties using the TSI 3563 integrating nephelometer. Aerosol Sci. Technol. 29, 57–69. https://doi.org/10.1080/02786829808965551.

Anderson, T.L., Covert, D.S., Wheeler, J.D., Harris, J.M., Perry, K.D., Trost, B.E., Jaffe, D. J., Ogren, J.A., 1999. Aerosol backscatter fraction and single scattering albedo: measured values and uncertainties at a coastal station in the Pacific Northwest. J. Geophys. Res. Atmos. 104, 26793–26807. https://doi.org/10.1029/1999JD900172.

Andrews, E., Sheridan, P.J., Fiebig, M., McComiskey, A., Ogren, J.A., Arnott, P., Covert, D., Elleman, R., Gasparini, R., Collins, D., Jonsson, H., Schmid, B., Wang, J., 2006a. Comparison of methods for deriving aerosol asymmetry parameter. J. Geophys. Res. Atmos. 111, D05S04. https://doi.org/10.1029/2004JD005734.

Andrews, E., Ogren, J.A., Bonasoni, P., Marinoni, A., Cuevas, E., Rodríguez, S., Sun, J.Y., Jaffe, D.A., Fischer, E.V., Baltensperger, U., Weingartner, E., Coen, M.C., Sharma, S., Macdonald, A.M., Leaitch, W.R., Lin, N.H., Laj, P., Arsov, T., Kalapov, I.,

Jefferson, A., Sheridan, P., 2011. Climatology of aerosol radiative properties in the free troposphere. Atmos. Res. 102, 365–393. https://doi.org/10.1016/j.atmosres.2011.08.017.

Ashbaugh, L.L., Malm, W.C., Sadeh, W.Z., 1985. A residence time probability analysis of sulfur concentrations at grand Canyon National Park. Atmos. Environ. 19, 1263–1270. https://doi.org/10.1016/0004-6981(85)90256-2.

Bäumer, D., Vogel, B., Versick, S., Rinke, R., Möhler, O., Schnaiter, M., 2008. Relationship of visibility, aerosol optical thickness and aerosol size distribution in an ageing air mass over South-West Germany. Atmos. Environ. 42, 989–998. https://doi.org/10.1016/j.atmosenv.2007.10.017.

Bond, T.C., Doherty, S.J., Fahey, D.W., Forster, P.M., Berntsen, T., DeAngelo, B.J., Flanner, M.G., Ghan, S., Kärcher, B., Koch, D., Kinne, S., Kondo, Y., Quinn, P.K., Sarofim, M.C., Schultz, M.G., Schulz, M., Venkataraman, C., Zhang, H., Zhang, S., Bellouin, N., Guttikunda, S.K., Hopke, P.K., Jacobson, M.Z., Kaiser, J.W., Klimont, Z., Lohmann, U., Schwarz, J.P., Shindell, D., Storelvmo, T., Warren, S.G., Zender, C.S., 2013. Bounding the role of black carbon in the climate system: a scientific assessment. J. Geophys. Res. Atmos. 118, 5380–5552. https://doi.org/10.1002/jgrd.50171.

Boucher, O., 2015. Atmospheric aerosols. In: Atmospheric Aerosols. Springer Netherlands, Dordrecht, pp. 9–24. https://doi.org/10.1007/978-94-017-9649-1_2.

Carslaw, D.C., Ropkins, K., 2012. Openair - an r package for air quality data analysis. Environ. Model. Software 27 (28), 52–61. https://doi.org/10.1016/j.envsoft.2011.09.008.

Charlson, R.J., Schwartz, S.E., Hales, J.M., Cess, R.D., Coakley, J.A., Hansen, J.E., Hofmann, D.J., 1992. Climate forcing by anthropogenic aerosols. Science 255, 423–430. https://doi.org/10.1126/science.255.5043.423.

Cherian, R., Quaas, J., Salzmann, M., Wild, M., 2014. Pollution trends over Europe constrain global aerosol forcing as simulated by climate models. Geophys. Res. Lett. 41, 2176–2181. https://doi.org/10.1002/2013GL058715.

Collaud Coen, Martine, Weingartner, E., Nyeki, S., Cozic, J., Henning, S., Verheggen, B., Gehrig, R., Baltensperger, U., 2007. Long-term trend analysis of aerosol variables at the high-alpine site Jungfraujoch. J. Geophys. Res. Atmos. 112, D13213 https://doi.org/10.1029/2006JD007995.

Colette, A., Granier, C., Hodnebrog Jakobs, H., Maurizi, A., Nyiri, A., Bessagnet, B., D'Angiola, A., D'Isidoro, M., Gauss, M., Meleux, F., Memmesheimer, M., Mieville, A., Roüil, L., Russo, F., Solberg, S., Stordal, F., Tampieri, F., 2011. Air quality trends in Europe over the past decade: a first multi-model assessment. Atmos. Chem. Phys. 11, 11657–11678. https://doi.org/10.5194/acp-11-11657-2011.

Collaud Coen, M., Andrews, E., Lastuey, A., Petkov Arsov, T., Backman, J., Brem, B.T., Bukowiecki, N., Couret, C., Eleftheriadis, K., Flentje, H., Fiebig, M., Gysel-Beer, M., Hand, J.L., Hoffer, A., Hooda, R., Hueglin, C., Joubert, W., Keywood, M., Eun Kim, J., Kim, S.W., Labuschagne, C., Lin, N.H., Lin, Y., Lund Myhre, C., Luoma, K., Lyamani, H., Marinoni, A., Mayol-Bracero, O.L., Mihalopoulos, N., Pandolfi, M., Prats, N., Prenni, A.J., Putaud, J.P., Ries, L., Reisen, F., Sellegri, K., Sharma, S., Sheridan, P., Patrick Sherman, J., Sun, J., Titos, G., Torres, E., Tuch, T., Weller, R., Wiedensohler, A., Zieger, P., Laj, P., 2020. Multidecadal trend analysis of in situ aerosol radiative properties around the world. Atmos. Chem. Phys. 20, 8867–8908. https://doi.org/10.5194/acp-20-8867-2020.

CSO, 2022. Population of Municipalities - 1 January 2020. CZSO [WWW Document]. Popul. Munic. URL. https://www.czso.cz/csu/czso/population-of-municipalities-1-january-2019, 2.1.23.

Delene, D.J., Ogren, J.A., 2002. Variability of aerosol optical properties at four North American surface monitoring sites. J. Atmos. Sci. 59, 1135–1150. https://doi.org/10.1175/1520-0469(2002)059<1135:VOAOPA>2.0.CO;2.

Donateo, A., Lo Feudo, T., Marinoni, A., Calidonna, C.R., Contini, D., Bonasoni, P., 2020. Long-term observations of aerosol optical properties at three GAW regional sites in the Central Mediterranean. Atmos. Res. 241, 104976 https://doi.org/10.1016/j.atmosres.2020.104976.

Draxler, Hess, 1998. An overview of the HYSPLIT_4 modelling system for trajectories dispersion and deposition. Aust. Meteorol. Mag. 47, 295–308.

Dvorská, A., Sedlák, P., Schwarz, J., Fusek, M., Hanuš, V., Vodička, P., Trusina, J., 2015. Atmospheric station Křešín u Pacova, Czech Republic – a Central European research infrastructure for studying greenhouse gases, aerosols and air quality. Adv. Sci. Res. 12, 79–83. https://doi.org/10.5194/asr-12-79-2015.

Eck, T.F., Holben, B.N., Reid, J.S., Dubovik, O., Smirnov, A., O'Neill, N.T., Slutsker, I., Kinne, S., 1999. Wavelength dependence of the optical depth of biomass burning, urban, and desert aerosols | Enhanced Reader. J. Geogr. Res. 104, 31333–31349. https://doi.org/10.1029/1999JD900923.

Elias, T., Haeffelin, M., Drobinski, P., Gomes, L., Rangognio, J., Bergot, T., Chazette, P., Raut, J.-C., Colomb, M., 2009. Particulate contribution to extinction of visible radiation: pollution, haze, and fog. Atmos. Res. 92, 443–454. https://doi.org/10.1016/j.atmosres.2009.01.006.

Ganguly, D., Jayaraman, A., Rajesh, T.A., Gadhavi, H., 2006. Wintertime aerosol properties during foggy and nonfoggy days over urban center Delhi and their implications for shortwave radiative forcing. J. Geophys. Res. 111, D15217 https://doi.org/10.1029/2005JD007029.

Ghan, S.J., 2013. Technical note: estimating aerosol effects on cloud radiative forcing. Atmos. Chem. Phys. 13, 9971–9974. https://doi.org/10.5194/acp-13-9971-2013.

Gopal, K.R., Arafath, S.M., Lingaswamy, A.P., Balakrishnaiah, G., Pavan Kumari, S., Uma Devi, K., Siva Kumar Reddy, N., Raja Obul Reddy, K., Penchal Reddy, M., Reddy, R. R., Suresh Babu, S., 2014. In-situ measurements of atmospheric aerosols by using Integrating Nephelometer over a semi-arid station, southern India. Atmos. Environ. https://doi.org/10.1016/j.atmosenv.2013.12.009.

Hansen, J., Sato, M., Ruedy, R., 1997. Radiative forcing and climate response. J. Geophys. Res. Atmos. 102, 6831–6864. https://doi.org/10.1029/96JD03436.

Hinds, W.C., 1999. Aerosol Technology, Properties, Behaviour, and Measurement of Airborne Particles. John Wiley & Sons Inc, New York.

Holubová Šmejkalová, A., Zíková, N., Ždímal, V., Plachá, H., Bitter, M., 2021. Atmospheric aerosol growth rates at different background station types. Environ. Sci. Pollut. Res. 28, 13352–13364. https://doi.org/10.1007/s11356-020-11424-5.

Isokääntä, S., Kim, P., Mikkonen, S., Kühn, T., Kokkola, H., Yli-Juuti, T., Heikkinen, L., Luoma, K., Petäjä, T., Kipling, Z., Partridge, D., Virtanen, A., 2022. The effect of clouds and precipitation on the aerosol concentrations and composition in a boreal forest environment. Atmos. Chem. Phys. 22, 11823–11843. https://doi.org/10.5194/acp-22-11823-2022.

IPCC, 2021. In: Masson-Delmotte, V., Zhai, P., Pirani, A., Connors, S.L., Péan, C., Berger, S., Caud, N., Chen, Y. (Eds.), Climate Change 2021: the Physical Science Basis. Contribution of Working Group I to the Sixth Assessment Report of the Intergovernmental Panel on Climate Change. Cambridge Univ. Press, p. 3949.

Kalmus, P., Ao, C.O., Wang, K.N., Manzi, M.P., Teixeira, J., 2022. A high-resolution planetary boundary layer height seasonal climatology from GNSS radio occultations. Remote Sens. Environ. 276, 113037 https://doi.org/10.1016/j.rse.2022.113037.

Kalnay, E., Kanamitsu, M., Kistler, R., Collins, W., Deaven, D., Gandin, L., Iredell, M., Saha, S., White, G., Woollen, J., Zhu, Y., Chelliah, M., Ebisuzaki, W., Higgins, W., Janowiak, J., Mo, K.C., Ropelewski, C., Wang, J., Leetmaa, A., Reynolds, R., Jenne, R., Joseph, D., 1996. The NCEP/NCAR 40-year reanalysis project. Bull. Am. Meteorol. Soc. 77, 437–471. https://doi.org/10.1175/1520-0477(1996)077<0437:TNYRP>2.0.CO;2.

Kim, K.Y., 2022. Diurnal and seasonal variation of planetary boundary layer height over East Asia and its climatic change as seen in the ERA-5 reanalysis data. SN Appl. Sci. 4, 39. https://doi.org/10.1007/s42452-021-04918-5.

Koolen, C.D., Rothenberg, G., 2019. Air pollution in Europe. ChemSusChem 12, 164–172. https://doi.org/10.1002/cssc.201802292.

Koschmieder, H., 1924. Theorie der horizontalen Sichtweite. Beiträge zur Phys. der freien Atmosphäre 12, 33–53.

Laj, P., Bigi, A., Rose, C., Andrews, E., Lund Myhre, C., Collaud Coen, M., Lin, Y., Wiedensohler, A., Schulz, M., A Ogren, J., Fiebig, M., Gliß, J., Mortier, A., Pandolfi, M., Petäja, T., Kim, S.W., Aas, W., Putaud, J.P., Mayol-Bracero, O., Keywood, M., Labrador, L., Aalto, P., Ahlberg, E., Alados Arboledas, L., Alastuey, A., Andrade, M., Artinano, B., Ausmeel, S., Arsov, T., Asmi, E., Backman, J., Baltensperger, U., Bastian, S., Bath, O., Paul Beukes, J., T Brem, B., Bukowiecki, N., Conil, S., Couret, C., Day, D., Dayantolis, W., Degorska, A., Eleftheriadis, K., Fetfatzis, P., Favez, O., Flentje, H., I Gini, M., Gregorič, A., Gysel-Beer, M., Gannet Hallar, A., Hand, J., Hoffer, A., Hueglin, C., K Hooda, R., Hyvärinen, A., Kalapov, I., Kalivitis, N., Kasper-Giebl, A., Eun Kim, J., Kouvarakis, G., Kranjc, I., Krejci, R., Kulmala, M., Labuschagne, C., Lee, H.J., Lihavainen, H., Lin, N.H., Löschau, G., Luoma, K., Marinoni, A., Martins Dos Santos, S., Meinhardt, F., Merkel, M., Metzger, J.M., Mihalopoulos, N., Anh Nguyen, N., Ondracek, J., Pérez, N., Rita Perrone, M., Pichon, J.M., Picard, D., Pichon, J.M., Pont, V., Prats, N., Prenni, A., Reisen, F., Romano, S., Sellegri, K., Sharma, S., Schauer, G., Sheridan, P., Patrick Sherman, J., Schütze, M., Schwerin, A., Sohmer, R., Sorribas, M., Steinbacher, M., Sun, J., Titos, G., Toczko, B., Tuch, T., Tulet, P., Tunved, P., Vakkari, V., Velarde, F., Velasquez, P., Villani, P., Vratolis, S., Wang, S.H., Weinhold, K., Weller, R., Yela, M., Yus-Diez, J., Zdimal, V., Zieger, P., Zikova, N., 2020. A global analysis of climate-relevant aerosol properties retrieved from the network of Global Atmosphere Watch (GAW) near-surface observatories. Atmos. Meas. Tech. 13, 4353–4392. https://doi.org/10.5194/amt-13-4353-2020.

Lee, L.A., Reddington, C.L., Carslaw, K.S., 2016. On the relationship between aerosol model uncertainty and radiative forcing uncertainty. Proc. Natl. Acad. Sci. 113, 5820–5827. https://doi.org/10.1073/pnas.1507050113.

Li, J., Carlson, B.E., Yung, Y.L., Lv, D., Hansen, J., Penner, J.E., Liao, H., Ramaswamy, V., Kahn, R.A., Zhang, P., Dubovik, O., Ding, A., Lacis, A.A., Zhang, L., Dong, Y., 2022. Scattering and absorbing aerosols in the climate system. Nat. Rev. Earth Environ. 3, 363–379. https://doi.org/10.1038/s43017-022-00296-7.

Luoma, K., Virkkula, A., Aalto, P., Petäjä, T., Kulmala, M., 2019. Over a 10-year record of aerosol optical properties at SMEAR II. Atmos. Chem. Phys. 19, 11363–11382. https://doi.org/10.5194/acp-19-11363-2019.

Mbengue, S., Fusek, M., Schwarz, J., Vodička, P., Šmejkalová, A.H., Holoubek, I., 2018. Four years of highly time resolved measurements of elemental and organic carbon at a rural background site in Central Europe. Atmos. Environ. 182, 335–346. https://doi.org/10.1016/j.atmosenv.2018.03.056.

Mbengue, S., Zikova, N., Schwarz, J., Vodička, P., Šmejkalová, A.H., Holoubek, I., 2021. Mass absorption cross-section and absorption enhancement from long term black and elemental carbon measurements: a rural background station in Central Europe. Sci. Total Environ. 794, 1–14. https://doi.org/10.1016/j.scitotenv.2021.148365.

Müller, T., Nowak, A., Wiedensohler, A., Sheridan, P., Laborde, M., Covert, D.S., Marinoni, A., Imre, K., Henzing, B., Roger, J.C., Dos Santos, S.M., Wilhelm, R., Wang, Y.Q., De Leeuw, G., 2009. Angular illumination and truncation of three different integrating nephelometers: implications for empirical, size-based corrections. Aerosol Sci. Technol. 43, 581–586. https://doi.org/10.1080/02786820902798484.

Myhre, G., Samset, B.H., Mohr, C.W., Alterskjær, K., Balkanski, Y., Bellouin, N., Chin, M., Haywood, J., Hodnebrog, O., Kinne, S., Lin, G., Lund, M.T., Penner, J.E., Schulz, M., Schutgens, N., Skeie, R.B., Stier, P., Takemura, T., Zhang, K., 2020. Cloudy-sky contributions to the direct aerosol effect. Atmos. Chem. Phys. 20, 8855–8865. https://doi.org/10.5194/acp-20-8855-2020.

NOAA Air Resources Laboratory, 2023. HYSPLIT model [WWW Document]. URL. https://www.ready.noaa.gov/HYSPLIT.php.

Noble, S.R., Hudson, J.G., 2019. Effects of continental clouds on surface Aitken and accumulation modes. J. Geophys. Res. Atmos. 124, 5479–5502. https://doi.org/10.1029/2019JD030297.

Ogren, J.A., Sheridan, P.J., Andrews, E., 2009. Cloud Scavenging Effects on Aerosol Radiative and Cloud-Nucleating Properties – Final Technical Report. U.S. Department of Commerce, National Oceanic and Atmospheric Administration, Earth System Research Laboratory.

Pandolfi, M., Alados-Arboledas, L., Alastuey, A., Andrade, M., Angelov, C., Artiñano, B., Backman, J., Baltensperger, U., Bonasoni, P., Bukowiecki, N., Collaud Coen, M., Conil, S., Coz, E., Crenn, V., Dudoitis, V., Ealo, M., Eleftheriadis, K., Favez, O., Fetfatzis, P., Fiebig, M., Flentje, H., Ginot, P., Gysel, M., Henzing, B., Hoffer, A., Holubova Smejkalova, A., Kalapov, I., Kalivitis, N., Kouvarakis, G., Kristensson, A., Kulmala, M., Lihavainen, H., Lunder, C., Luoma, K., Lyamani, H., Marinoni, A., Mihalopoulos, N., Moerman, M., Nicolas, J., O'Dowd, C., Petäjä, T., Petit, J.E., Marc Pichon, J., Prokopciuk, N., Putaud, J.P., Rodríguez, S., Sciare, J., Sellegri, K., Swietlicki, E., Titos, G., Tuch, T., Tunved, P., Ulevicius, V., Vaishya, A., Vana, M., Virkkula, A., Vratolis, S., Weingartner, E., Wiedensohler, A., Laj, P., 2018. A European aerosol phenomenology - 6: scattering properties of atmospheric aerosol particles from 28 ACTRIS sites. Atmos. Chem. Phys. 18, 7877–7911. https://doi.org/10.5194/acp-18-7877-2018.

Perrone, M.R., Genga, A., Siciliano, M., Siciliano, T., Paladini, F., Burlizzi, P., 2016. Saharan dust impact on the chemical composition of PM10 and PM1 samples over south-eastern Italy. Arab. J. Geosci. 9, 1–11. https://doi.org/10.1007/s12517-015-2227-3.

Perrone, M.R., Romano, S., Genga, A., Paladini, F., 2018. Integration of optical and chemical parameters to improve the particulate matter characterization. Atmos. Res. 205, 93–106. https://doi.org/10.1016/j.atmosres.2018.02.015.

Qin, K., Wang, L., Xu, J., Letu, H., Zhang, K., Li, D., Zou, J., Fan, W., 2018. Haze optical properties from long-term ground-based remote sensing over Beijing and Xuzhou, China. Rem. Sens. 10, 518. https://doi.org/10.3390/rs10040518.

Quaas, J., Arola, A., Cairns, B., Christensen, M., Deneke, H., Ekman, A.M.L., Feingold, G., Fridlind, A., Gryspeerdt, E., Hasekamp, O., Li, Z., Lipponen, A., Mülmenstädt, J., Nenes, A., Penner, J.E., Rosenfeld, D., Schrödner, R., Sinclair, K., Sourdeval, O., Stier, P., Tesche, M., Van Diedenhoven, B., Wendisch, M., 2020. Constraining the Twomey effect from satellite observations: issues and perspectives. Atmos. Chem. Phys. 20, 15079–15099. https://doi.org/10.5194/acp-20-15079-2020.

Quaas, J., Jia, H., Smith, C., Albright, A.L., Aas, W., Bellouin, N., Boucher, O., Doutriaux-Boucher, M., Forster, P.M., Grosvenor, D., Jenkins, S., Klimont, Z., Loeb, N.G., Ma, X., Naik, V., Paulot, F., Stier, P., Wild, M., Myhre, G., Schulz, M., 2022. Robust evidence for reversal of the trend in aerosol effective climate forcing. Atmos. Chem. Phys. 22, 12221–12239. https://doi.org/10.5194/acp-22-12221-2022.

R Core Team, 2020. R: a language and environment for statistical computing [WWW Document]. URL. https://www.r-project.org/, 4.10.23.

Rajesh, T.A., Ramachandran, S., 2020. Extensive and intensive properties of aerosol over distinct environments: influence of anthropogenic emissions and meteorology. J. Atmos. Sol. Terr. Phys. 202, 105223 https://doi.org/10.1016/j.jastp.2020.105223.

Rama Gopal, K., Arafath, S.M., Lingaswamy, A.P., Balakrishnaiah, G., Pavan Kumari, S., Uma Devi, K., Siva Kumar Reddy, N., Raja Obul Reddy, K., Penchal Reddy, M., Reddy, R.R., Suresh Babu, S., 2014. In-situ measurements of atmospheric aerosols by using Integrating Nephelometer over a semi-arid station, southern India. Atmos. Environ. 86, 228–240. https://doi.org/10.1016/j.atmosenv.2013.12.009.

Ramanathan, V., Crutzen, P.J., Kiehl, J.T., Rosenfeld, D., 2001. Atmosphere: aerosols, climate, and the hydrological cycle. Science 294, 2119–2124. https://doi.org/10.1126/science.1064034.

Ramonet, M., Ciais, P., Apadula, F., Bartyzel, J., Bastos, A., Bergamaschi, P., Blanc, P.E., Brunner, D., Carracciolo di Torchiarolo, L., Calzolari, F., Chen, H., Chmura, L., Colomb, A., Conil, S., Cristofanelli, P., Cuevas, E., Curcoll, R., Delmotte, M., di Sarra, A., Emmenegger, L., Forster, G., Frumau, A., Gerbig, C., Gheusi, F., Hammer, S., Haszpra, L., Hatakka, J., Hazan, L., Heliasz, M., Henne, S., Hensen, A., Hermansen, O., Keronen, P., Kivi, R., Komínková, K., Kubistin, D., Lurent, O., Laurila, T., Lavric, J.V., Lehner, I., Lehtinen, K.E.J., Leskinen, A., Leuenberger, M., Levin, I., Lindauer, M., Lopez, M., Lund Myhre, M., Mammarella, I., Manca, G., Manning, A., Marek, M.V., Marklund, P., Martin, D., Meinhardt, F., Mihalopoulos, N., Molder, M., Morgui, J.A., Necki, J., O'Doherty, S., O'Dowd, C., Ottosson, M., Philippon, C., Piacentino, S., Pichon, J.M., Plass-Duelmer, C., Resovsky, A., Rivier, L., Rodó, X., Sha, M.K., Scheeren, H.A., Sferlazzo, D., Spain, T. G., Stanley, K.M., Steinbacher, M., Trisolino, P., Vermeulen, A., Vítková, G., Weyrauch, D., Xueref-Remy, I., Yala, K., Yver Kwork, C., 2020. The fingerprint of the summer 2018 drought in Europe on ground-based atmospheric CO2 measurements Enhanced Reader. Phil. Trans. B, 20190513.

Rolph, G., Stein, A., Stunder, B., 2017. Real-time environmental applications and display sYstem: READY. Environ. Model. Software 95, 210–228. https://doi.org/10.1016/j.envsoft.2017.06.025.

RSD, 2020. Sčítání dopravy - ŘSD ČR [WWW Document]. URL. https://www.rsd.cz/silnice-a-dalnice/scitani-dopravy#zalozka-celostatni-scitani-dopravy-2020, 2.1.23.

Safai, P.D., Ghude, S., Pithani, P., Varpe, S., Kulkarni, R., Todekar, K., Tiwari, S., Chate, D.M., Prabhakaran, T., Jenamani, R.K., Rajeevan, M.N., 2019. Two-way relationship between aerosols and fog: a case study at IGI Airport, New Delhi. Aerosol Air Qual. Res. 19, 71–79. https://doi.org/10.4209/aaqr.2017.11.0542.

Schmeisser, L., Backman, J., Ogren, J.A., Andrews, E., Asmi, E., Starkweather, S., Uttal, T., Fiebig, M., Sharma, S., Eleftheriadis, K., Vratolis, S., Bergin, M., Tunved, P., Jefferson, A., 2018. Seasonality of aerosol optical properties in the Arctic. Atmos. Chem. Phys. 18, 11599–11622. https://doi.org/10.5194/acp-18-11599-2018.

Schuster, G.L., Dubovik, O., Holben, B.N., 2006. Angstrom exponent and bimodal aerosol size distributions. J. Geophys. Res. 111, D07207 https://doi.org/10.1029/2005JD006328.

Schwarz, J., Cusack, M., Karban, J., Chalupníčková, E., Havránek, V., Smolík, J., Ždímal, V., 2016. PM2.5 chemical composition at a rural background site in Central Europe, including correlation and air mass back trajectory analysis. Atmos. Res. 176–177, 108–120. https://doi.org/10.1016/j.atmosres.2016.02.017.

Seinfeld, J.H., Pandis, S.N., 2006. Atmospheric chemistry and physics. In: Fundamentals of Physics and Chemistry of the Atmosphere, second ed. John Wiley & Sons, Ltd, New Jersey. https://doi.org/10.1007/978-3-662-04540-4_16.

Shahpoury, P., Lammel, G., Šmejkalová, A.H., Klánová, J., Přibylová, P., Váňa, M., 2015. Polycyclic aromatic hydrocarbons, polychlorinated biphenyls, and chlorinated pesticides in background air in central Europe - investigating parameters affecting wet scavenging of polycyclic aromatic hydrocarbons. Atmos. Chem. Phys. 15, 1795–1805. https://doi.org/10.5194/acp-15-1795-2015.

Sheridan, P.J., Delene, D.J., Ogren, J.A., 2001. Four years of continuous surface aerosol measurements from the department of energy's atmospheric radiation measurement program southern great plains cloud and radiation testbed site. J. Geophys. Res. Atmos. 106, 20735–20747. https://doi.org/10.1029/2001JD000785.

Sierau, B., Covert, D.S., Coffman, D.J., Quinn, P.K., Bates, T.S., 2006. Aerosol optical properties during the 2004 new England air quality study-intercontinental transport and chemical transformation: gulf of Maine surface measurements-regional and case studies. J. Geophys. Res. Atmos. 111, D23S37. https://doi.org/10.1029/2006JD007568.

Šmejkalová, A.H., Brzezina, J., 2022. The effect of drought on PM concentrations in the Czech Republic. Aerosol Air Qual. Res. 22, 220130 https://doi.org/10.4209/aaqr.220130.

Stein, A.F., Draxler, R.R., Rolph, G.D., Stunder, B.J.B., Cohen, M.D., Ngan, F., 2015. Noaa's hysplit atmospheric transport and dispersion modeling system. Bull. Am. Meteorol. Soc. 96, 2059–2077. https://doi.org/10.1175/BAMS-D-14-00110.1.

The European Parliament, The Council of the European union, 2008. DIRECTIVE 2008/50/EC OF THE EUROPEAN PARLIAMENT AND OF THE COUNCIL of 21 May 2008 on ambient air quality and cleaner air for Europe. Off. J. Eur. Union 44.

Thornhill, G.D., Collins, W.J., Kramer, R.J., Olivie, D., Skeie, R.B., O'Connor, F.M., Luke Abraham, N., Checa-Garcia, R., Bauer, S.E., Deushi, M., Emmons, L.K., Forster, P.M., Horowitz, L.W., Johnson, B., Keeble, J., Lamarque, J.F., Michou, M., Mills, M.J., Mulcahy, J.P., Myhre, G., Nabat, P., Naik, V., Oshima, N., Schulz, M., Smith, C.J., Takemura, T., Tilmes, S., Wu, T., Zeng, G., Zhang, J., 2021. Effective radiative forcing from emissions of reactive gases and aerosols-A multi-model comparison. Atmos. Chem. Phys. 21, 853–874. https://doi.org/10.5194/acp-21-853-2021.

Titos, G., Foyo-Moreno, L., Lyamani, H., Querol, X., Alastuey, A., Alados-Arboledas, L., 2012. Optical properties and chemical composition of aerosol particles at an urban location: an estimation of the aerosol mass scattering and absorption efficiencies. J. Geophys. Res. 117, D04206 https://doi.org/10.1029/2011JD016671.

Tiwari, S., Pandithurai, G., Attri, S.D., Srivastava, A.K., Soni, V.K., Bisht, D.S., Anil Kumar, V., Srivastava, M.K., 2015. Aerosol optical properties and their relationship with meteorological parameters during wintertime in Delhi, India. Atmos. Res. 153, 465–479. https://doi.org/10.1016/j.atmosres.2014.10.003.

Uria-Tellaetxe, I., Carslaw, D.C., 2014. Conditional bivariate probability function for source identification. Environ. Model. Software 59, 1–9. https://doi.org/10.1016/j.envsoft.2014.05.002.

Van Dingenen, R., Raes, F., Putaud, J.P., Baltensperger, U., Charron, A., Facchini, M.C., Decesari, S., Fuzzi, S., Gehrig, R., Hansson, H.C., Harrison, R.M., Hüglin, C., Jones, A.M., Laj, P., Lorbeer, G., Maenhaut, W., Palmgren, F., Querol, X., Rodriguez, S., Schneider, J., Ten Brink, H., Tunved, P., Tørseth, K., Wehner, B., Weingartner, E., Wiedensohler, A., Wåhlin, P., 2004. A European aerosol phenomenology - 1: physical characteristics of particulate matter at kerbside, urban, rural and background sites in Europe. Atmos. Environ. 38, 2561–2577. https://doi.org/10.1016/j.atmosenv.2004.01.040.

Vodička, P., Schwarz, J., Cusack, M., Ždímal, V., 2015. Detailed comparison of OC/EC aerosol at an urban and a rural Czech background site during summer and winter. Sci. Total Environ. 518–519, 424–433. https://doi.org/10.1016/j.scitotenv.2015.03.029.

Wang, Y., Le, T., Chen, G., Yung, Y.L., Su, H., Seinfeld, J.H., Jiang, J.H., 2020. Reduced European aerosol emissions suppress winter extremes over northern Eurasia. Nat. Clim. Change 10, 225–230. https://doi.org/10.1038/s41558-020-0693-4.

Wiscombie, W.J., Grams, G.W., 1976. Backscattered fraction in two-stream approximations. J. Atmos. Sci. 33, 2440–2451. https://doi.org/10.1175/1520-0469(1976)033<2440:tbfits>2.0.co;2.

Zhang, M., Liu, J., Bilal, M., Zhang, C., Nazeer, M., Atique, L., Han, G., Gong, W., 2020. Aerosol optical properties and contribution to differentiate haze and haze-free weather in Wuhan city. Atmosphere (Basel) 11, 322. https://doi.org/10.3390/atmos11040322.

Zíková, N., Ždímal, V., 2013. Long-term measurement of aerosol number size distributions at rural background station Košetice. Aerosol Air Qual. Res. 13, 1464–1474. https://doi.org/10.4209/aaqr.2013.02.0056.

Zíková, N., Ždimal, V., 2016. Precipitation scavenging of aerosol particles at a rural site in the Czech Republic. Tellus Ser. B Chem. Phys. Meteorol. 68, 27343 https://doi.org/10.3402/tellusb.v68.27343.

Zíková, N., Wang, Y., Yang, F., Li, X., Tian, M., Hopke, P.K., 2016. On the source contribution to Beijing PM 2.5 concentrations. Atmos. Environ. 134, 84–95. https://doi.org/10.1016/j.atmosenv.2016.03.047.